*Publ. Astron. Soc. Japan* (2016) 68 (1), 5 (1–14)
doi: 10.1093/pasj/psv108
Advance Access Publication Date: 2015 November 19

# Three-dimensional distribution of the ISM in the Milky Way galaxy. III. The total neutral gas disk

**Hiroyuki NAKANISHI[1,2,*] and Yoshiaki SOFUE[3]**

[1]Graduate Schools of Science and Engineering, Kagoshima University, 1-21-35 Korimoto, Kagoshima, Kagoshima 890-0065, Japan
[2]Institute of Space and Astronautical Science, Japan Aerospace Exploration Agency, 3-1-1 Yoshinodai, Chuo-ku, Sagamihara, Kanagawa 252-5210, Japan
[3]Institute of Astronomy, The University of Tokyo, 2-21-1 Osawa, Mitaka, Tokyo 181-0015, Japan

*E-mail: hnakanis@sci.kagoshima-u.ac.jp

Received 2015 August 17; Accepted 2015 October 6

## Abstract

We present newly obtained three-dimensional gaseous maps of the Milky Way Galaxy: H I, $H_2$, and total-gas (H I plus $H_2$) maps, which were derived from the H I and $^{12}$CO($J=1$–0) survey data and rotation curves based on the kinematic distance. The H I and $H_2$ face-on maps show that the H I disk is extended to a radius of 15–20 kpc and its outskirts are asymmetric to the Galactic center, while most of the $H_2$ gas is distributed inside the solar circle. The total gas mass within a radius of 30 kpc amounts to $8.0 \times 10^9\ M_\odot$, 89% and 11% of which are H I and $H_2$, respectively. The vertical slices show that the outer H I disk is strongly warped and the inner H I and $H_2$ disks are corrugated. The total gas map is advantageous for tracing spiral structures from the inner to outer disk. Spiral structures such as the Norma–Cygnus, the Perseus, the Sagittarius–Carina, the Scutum–Crux, and the Orion arms are more clearly traced in the total gas map than ever. All the spiral arms are well explained by logarithmic spiral arms with pitch angles of 11°–15°. The molecular fraction of the total gas is high near the Galactic center and decreases with Galactocentric distance. The molecular fraction is also locally enhanced at the spiral arms compared with the inter-arm regions.

**Key words:** Galaxy: disk — Galaxy: kinematics and dynamics — Galaxy: structure — ISM: kinematics and dynamics — radio lines: ISM

## 1 Introduction

The interstellar medium (ISM) is one of the major components of the Galaxy and consists of coronal gas, intercloud gas, diffuse clouds, dark clouds, Bok globules, molecular clouds, and H II regions (Myers 1978). The neutral hydrogen H I radiates a 1420 MHz line and traces intercloud gas, diffuse clouds, and dark clouds. Though the dominant component of molecular clouds is $H_2$ gas, it does not have an emission line in the radio wavelength range. Therefore, in general, carbon monoxide molecule CO line is used as a tracer of $H_2$ gas, and $H_2$ gas density is calculated with a conversion factor $X_{\rm CO}$.

All-sky H I and CO line survey data at radio wavelengths are great tools to reveal the Galactic global structure, because (1) the radio signal suffers relatively low extinction due to its long wavelength, (2) neutral hydrogen and molecular gases observed in the radio lines are distributed over the whole Galaxy, and (3) the line data provide us with information about distances using a kinematic distance method.

There have been a lot of efforts to conduct H I and CO line surveys for the Galaxy. Muller and Westerhout (1957) carried out the Kootwijk H I survey with a 7.5 m telescope, with which Oort, Kerr, and Westerhout (1958) constructed the H I distribution map and found spiral structures such as the Sagittarius, the Orion (Local), and the Perseus arms. Succeeding works on H I surveys found more spiral structures such as the Cygnus (Outer) arm by analyzing the longitude–velocity (LV) diagram (Kerr 1969; Weaver 1970; Verschuur 1973). The latest H I survey conducted with Australia Telescope Compact Array showed that there exist additional spiral structures at the end of the H I disk in the fourth quadrant (McClure-Griffiths et al. 2004).

Dame et al. (1987) and Bronfman et al. (1988) carried out a $^{12}$CO($J=1$–0) line survey for the Galactic plane with a 1.2 m telescope, with which the Sagittarius and Carina arms were clearly traced by locating giant molecular clouds in the Galactic plane (Cohen et al. 1985; Dame et al. 1986; Myers et al. 1986; Grabelsky et al. 1987). Sanders et al. (1986) carried out a CO survey for the first quadrant of the Galaxy with a 14 m telescope and traced the Sagittarius and Perseus arms. Using the same CO survey data, Clemens, Sanders, and Scoville (1988) derived a face-on map of the molecular cloud distribution in the first quadrant. The latest study identified a new distant molecular spiral arm in the first quadrant, which is considered to be a continuation of the Scutum–Crux arm (Dame & Thaddeus 2011).

These spiral arms are identified with those in many other tracers such as H II regions (Georgelin & Georgelin 1976; Downes et al. 1980), thermal electrons (Taylor & Cordes 1993), dust emission (Drimmel & Spergel 2001), $^{26}$Al (Chen et al. 1996), synchrotron emission (Beuermann et al. 1985), and methanol masers (Caswell et al. 2011) besides the H I and CO studies. Vallée (2005) compiled studies of measurements of spiral arms published from 1980 to early 2005 for the meta-analysis of the Galactic spiral structure and presented spiral arms. Most studies have identified four spiral arms, whose shapes are concluded to be logarithmic spiral arms with pitch angles of $13.^{\circ}1 \pm 0.^{\circ}6$ (Vallée 2015).

In Paper I (Nakanishi & Sofue 2003) and Paper II (Nakanishi & Sofue 2006) we derived H I and $H_2$ gas maps using the latest H I (Hartmann & Burton 1997; Kerr et al. 1986; Burton & Liszt 1983) and CO survey data (Dame et al. 2001), and rotation curves (Clemens 1985; Dehnen & Binney 1998), based on the kinematic distance method. In these papers, we showed individual three-dimensional maps of H I and $H_2$ disks. The H I gas is widely distributed in the Galactic disk and it is extended further beyond the edge of the stellar disk. The surface density of the H I gas is larger in the outer Galaxy than in the inner Galaxy. On the other hand, most of the $H_2$ gas is distributed within the stellar disk. Therefore, the H I data is advantageous in investigating the structure of the outer Galaxy, while the CO data is suitable for examining the inner Galaxy.

In this paper we present total gas maps as well as H I and $H_2$ as the third part of this series. The total gas map is suitable for investigating the entire structure of the Galaxy from the inner to the outer parts. At the same time, we revise the H I map using the newly released LAB survey data (Kalberla et al. 2005); this was published after Paper I, and it has been found that the data analysis method could be improved through the work of Paper II.

We choose a Cartesian coordinate whose $x$-axis coincides with the line crossing the Sun and the Galactic center, and whose origin coincides with the Galactic center. The $z$-axis is chosen to be parallel to the rotational axis. We define that the Sun is located at ($-8$ kpc, 0, 0). We also use cylindrical coordinates ($R$, $\theta$, $z$) so that the angle $\theta = 180^{\circ}$ coincides with the direction toward the Sun and the angle $\theta = 90^{\circ}$ is parallel to $l = 90^{\circ}$. The Galactic constants $R_0 = 8.0$ kpc (the Galactocentric distance of the Sun) and $V_0 = 217\,\mathrm{km\,s^{-1}}$ (the solar rotational velocity) are adopted (Dehnen & Binney 1998).

## 2 Data

H I survey data were taken from the LAB (Leiden–Argentine–Bonn) survey (Kalberla et al. 2005), which consists of two survey data sets: the Leiden/Dwingeloo Survey conducted with the Leiden 25 m telescope whose half-power-beam-width (HPBW) was $0.^{\circ}6$ covering the northern sky of $\delta \geq -30^{\circ}$ (Hartmann & Burton 1997), and the Instituto Argentino de Radioastronomia Survey conducted with a 30 m telescope whose HPBW was $0.^{\circ}5$ covering the southern sky of $\delta \leq -25^{\circ}$ (Bajaja et al. 2005). The map grid spacing was $0.^{\circ}5$, which corresponded to a linear scale of 17 pc at the heliocentric distance of 1 kpc, the LSR (local standard of rest) velocity coverage ranged from $-450\,\mathrm{km\,s^{-1}}$ to $+400\,\mathrm{km\,s^{-1}}$ at a resolution of $1.3\,\mathrm{km\,s^{-1}}$, and the rms noise in the brightness temperature was 0.07–0.09 K. Residual systematic errors were reported as below 0.02–0.04 K. In Paper I, we used only spectra within the latitude range of $|\delta| \leq 10^{\circ}$ because the data for the southern hemisphere covered only $|\delta| \leq 10^{\circ}$. However, here we used spectra in the latitude range of $|\delta| \leq 30^{\circ}$, which covers more than 99% of the entire gaseous disk if we assume it is a cylinder with a radius of 20 kpc and thickness of 2 kpc.

CO survey data, which are used to derive $H_2$ gas distribution, were adopted from Dame, Hartmann, and Thaddeus (2001), who compiled CO survey data from Grabelsky et al. (1987), Bronfman et al. (1989), May et al. (1993), and Bitran et al. (1997) as described in Paper II. The data were obtained with 1.2 m telescopes in the USA and Chile. The HPBW was $8.'4$–$8.'8$, which corresponds to

2.4–2.5 pc at the heliocentric distance of 1 kpc. The map grid spacing was either $1/8^\circ$ or $1/4^\circ$ depending on the survey area. The LSR velocity coverage was 332 km s$^{-1}$ and the velocity resolution was 1.3 km s$^{-1}$. The rms noise in the brightness temperature was 0.12–0.43 K. The Galactic latitude range is $|b| \leq 1^\circ.5$. Since most of the molecular gas is distributed inside the solar circle and the FWHM (full width at half maximum) of the molecular disk is typically 100 pc, most of the CO gas is covered with spectra in this range.

The rotation curve data are also the same as those we used in Papers I and II. The outer rotation curve ($R > R_0$) was taken from Dehnen and Binney (1998), who presented model rotation curves fitted to the observation data available. The outer rotation curve we adopted is the best-fitting model among them. The Galactic constant $R_0 = 8.0$ kpc and $V_0 = 217$ km s$^{-1}$ are adopted in this model. The inner rotation curve ($R < R_0$) was taken from Clemens (1985), which was derived from the terminal velocity traced with the Massachusetts–Stoney Brook Galactic equator CO survey data. Though the original rotation curve was fitted with a polynomial function adopting Galactic constants of ($R_0$, $V_0$) = (8.5 kpc, 220 km s$^{-1}$) and (10 kpc, 250 km s$^{-1}$), we modified the constants of the polynomial function for the case of ($R_0$, $V_0$) = (8.0 kpc, 217 km s$^{-1}$) in order to connect smoothly to the outer rotation as described in Paper I.

## 3 Derivations of H I, $H_2$, and total gas maps

### 3.1 Kinematic distance

Assuming that the gases circularly rotate around the Galactic center without non-circular motion and that the rotational velocity is constant against the height from the Galactic plane, the heliocentric distance $r$ of H I and CO gases were calculated based on the kinematic distance as follows.

The LSR velocity $V_{\rm LSR}$ of the gas component observed in the direction ($l$, $b$) rotating at the Galactocentric distance $R$ is given by the equation

$$V_{\rm LSR} = \left[\frac{R_0}{R}V(R) - V_0\right]\sin l \cos b. \tag{1}$$

The heliocentric distance $r$ of the gas component can be given by solving the following relation between $r$, $R$, and $R_0$:

$$R^2 = r^2 + R_0^2 - 2r R_0 \cos l. \tag{2}$$

In the case of the outer Galaxy ($R > R_0$), the heliocentric distance is uniquely determined to be $r = R_0 \cos l + \sqrt{R^2 - R_0^2 \sin^2 l}$, while it has two solutions $r = R_0 \cos l \pm \sqrt{R^2 - R_0^2 \sin^2 l}$ for a given LSR velocity in the case of the inner Galaxy. However, there is no ambiguity at the tangential point $R = R_0 \sin l$, where the LSR velocity reaches a maximum, which is referred to as the terminal velocity $V_{\rm t}$, and the heliocentric distance is given by $r = R_0 \cos l$.

### 3.2 H I and $H_2$ distributions in the outer Galaxy

In the case of the outer Galaxy, the heliocentric distance can be uniquely determined as explained in the previous subsection. As described in Papers I and II, volume number densities $n$ [cm$^{-1}$] of H I and $H_2$ gases at the heliocentric distance $r$ in the direction ($l$, $b$) are calculated using the equation

$$n = XT_{\rm b}\frac{\Delta V_{\rm r}}{\Delta r}, \tag{3}$$

where $X$ is the conversion factor, for which we adopt $X = 1.82 \times 10^{18}$ (H cm$^{-2}$ K$^{-1}$ km$^{-1}$ s) for H I and $X = 1.8 \times 10^{20}$ ($H_2$ cm$^{-2}$ K$^{-1}$ km$^{-1}$ s) for $H_2$ gases (Dame et al. 2001), respectively. As described in Paper II, it is known that the conversion factor is likely to increase with Galactocentric distance (Arimoto et al. 1996). Therefore, the column density estimated in this paper might be overestimated around the Galactic center and underestimated for the outer Galaxy. The $H_2$ map obtained by adopting the conversion factor $X$ taken from Arimoto, Sofue, and Tsujimoto (1996) is shown in Paper II.

### 3.3 H I distribution in the inner Galaxy

In the case of the inner Galaxy, there is a near–far ambiguity in that there are two points ($r_1$, $r_2$) giving the same LSR velocity $V_{\rm LSR}$ in a single line-of-sight as explained in subsection 3.1. In order to solve this problem, we introduced a model of vertical density distribution at $r_i$ (Spitzer 1942):

$$n_i(z) = n_{0i}\,{\rm sech}^2\left[\ln(1+\sqrt{2})\frac{z - z_{0i}}{z_{1/2}}\right], \tag{4}$$

where $z_{0i}$ is the height of a midplane from the plane of $b = 0^\circ$, $n_{0i}$ is the volume density at the midplane, and $z_{1/2}$ is half the FWHM of the vertical gas distribution.

Adopting this model, the observed column density $N(b)$ is given as a function of Galactic latitude $b$ with the above model by

$$N(b)\cos b = n_1(r_1 \tan b)\Delta r_1 + n_2(r_2 \tan b)\Delta r_2, \tag{5}$$

where the subscripts 1 and 2 denote the near and far points, respectively.

Since the thickness of the gas layer $z_{1/2}$ primarily depends on the Galactocentric distance, for a given LSR velocity, the unknown parameters are $n_{01}$, $n_{02}$, $z_{01}$, and $z_{02}$, which we

can estimate by fitting the model function to the data. The search range of $z_{01}$ and $z_{02}$ is restricted to $|z| < 250$ pc as described in Paper II. To eliminate ill-fitting results giving artificial structures, we smoothed the obtained distance–density curve using a spline function and clipping points with large deviations.

### 3.4 Vertical profile of H I and $H_2$ gases at the tangential point

Before applying the fitting method described in the previous subsection, we measured the thickness of the gas disk layer by analyzing the vertical ($z$-direction) profile of H I and $H_2$ gases at the tangential point, where the kinematic distance is uniquely determined for a given LSR velocity. Since the H I gas with an LSR velocity in the range $|V_t| - \sigma \leq |V_{LSR}| \leq |V_t|$ contributes to a higher velocity component than the terminal velocity due to the velocity dispersion $\sigma$, H I volume density was calculated by integrating the emission within the velocity range of $|V_t| - \sigma \leq |V_{LSR}| \leq \infty$ adopting $\sigma = 5\,\mathrm{km\,s^{-1}}$ (Clemens 1985). Details are described in Papers I and II.

In the case of the outer Galaxy, the thickness was measured for all the points where a vertical H I profile was obtained.

The thickness $z_{1/2}$ was measured by fitting the model function to the observed vertical distributions. The measured FWHM ($2z_{1/2}$) of each gas layer is presented in subsection 4.4.

### 3.5 Regridding the obtained H I and $H_2$ distributions

As described above, we obtained H I and $H_2$ density cubes in the form $n_{H\,I}(l, b, r)$ and $n_{H_2}(l, b, r)$ from the line spectra cube $T_b(l, b, V_{LSR})$. Finally, these data cubes in the $(l, b, r)$ coordinates were transformed into $(x, y, z)$ coordinates as explained in section 1.

For the outer Galaxy, the data were regridded by interpolating the nearest points. For the inner Galaxy, first the parameter sets of $z_0$ (midplane height) and $n_0$ (midplane density) were regridded by averaging those surrounding a certain point with a weight function exponentially decreasing with an FWHM of 0.48 kpc, as described in Paper II.

The foreground H I emission surrounding the Sun having an LSR velocity of $V_{LSR} \sim 0\,\mathrm{km\,s^{-1}}$ can contribute to density distribution around the solar circle $R = R_0$ where the gas gives as LSR velocity of $0\,\mathrm{km\,s^{-1}}$. To avoid this artificial effect, the data were regridded in the same way as the inner Galaxy for the region of $|V_{LSR}|$ less than $3\,\sigma$, instead of the simple interpolation used for the outer Galaxy.

### 3.6 Revision of H I map

In this paper, the H I distribution map is revised. The following points were revised: (1) the search range of $z_0$ is restricted to $-250$–$+250$ pc, as in Paper II, in calculating H I distribution in the inner Galaxy; (2) the parameter sets $(n_0, z_0)$ obtained for the discrete points in the inner Galaxy were averaged with a Gaussian function whose FWHM was 0.48 kpc in order to regrid the H I distribution data; and (3) the flare component of the outer H I disk is not subtracted. Due to (1) and (2), artificial structures seen at high altitude in the inner Galaxy were able to be suppressed and the averaged surface density is not affected. Due to (3), the estimation of H I mass changed by factor of 2. In Paper I, most of the high-altitude emission was considered to be contributed by the local gas and this component was subtracted, assuming that the local gas could be expressed by a linear function of the Galactic latitude $b$. Hence, the H I density at the midplane was also underestimated in this process. The $H_2$ distribution map is taken from Paper II without revision.

## 4 New H I, $H_2$, and total gas maps

### 4.1 Face-on maps

Figure 1 shows contour maps of the resulting H I and $H_2$ column densities in the face-on view. The data range $|\theta| < 30^\circ$ (i.e., behind the Galactic Center) was masked because the data points are too sparse to make a map as described in Paper II. The global features such as spiral arms are consistent with previous works (Nakanishi & Sofue 2003, 2006).

The $H_2$ gas is concentrated in the inner region ($\lesssim R_0$ kpc) and is hardly detectable in the outer region. On the other hand, the H I gas is distributed from the center to the outer region ($\gtrsim R_0$ kpc). The lowest contour of 1 $M_\odot\,\mathrm{pc^{-2}}$, which is often referred to as the radius of the gaseous disk (Broeils & van Woerden 1994), shows that the radius is 15–20 kpc and that the outskirts are not axisymmetric. The H I disk swells in the direction of $\theta = -45^\circ$ if we assume a pure circular rotation. It is also shown that the disk is unnaturally asymmetric about $l = 180^\circ$. It is likely that the outermost disk does not rotate circularly with the outer disk.

Next, we show comparisons of H I and $H_2$ in figure 2. The top panel of figure 2 is a false color image showing H I and $H_2$ in red and green, respectively. This figure shows clearly that H I and $H_2$ gases are dominant in the outer and inner parts, respectively. The gas phase transition from H I to $H_2$ occurs within a narrow range of radius around $R_0$, which is referred to as the molecular front (Sofue et al. 1995; Honma et al. 1995).

The bottom panel of figure 2 is a total (H I plus $H_2$) gas map, which is presented for the first time by obtaining both

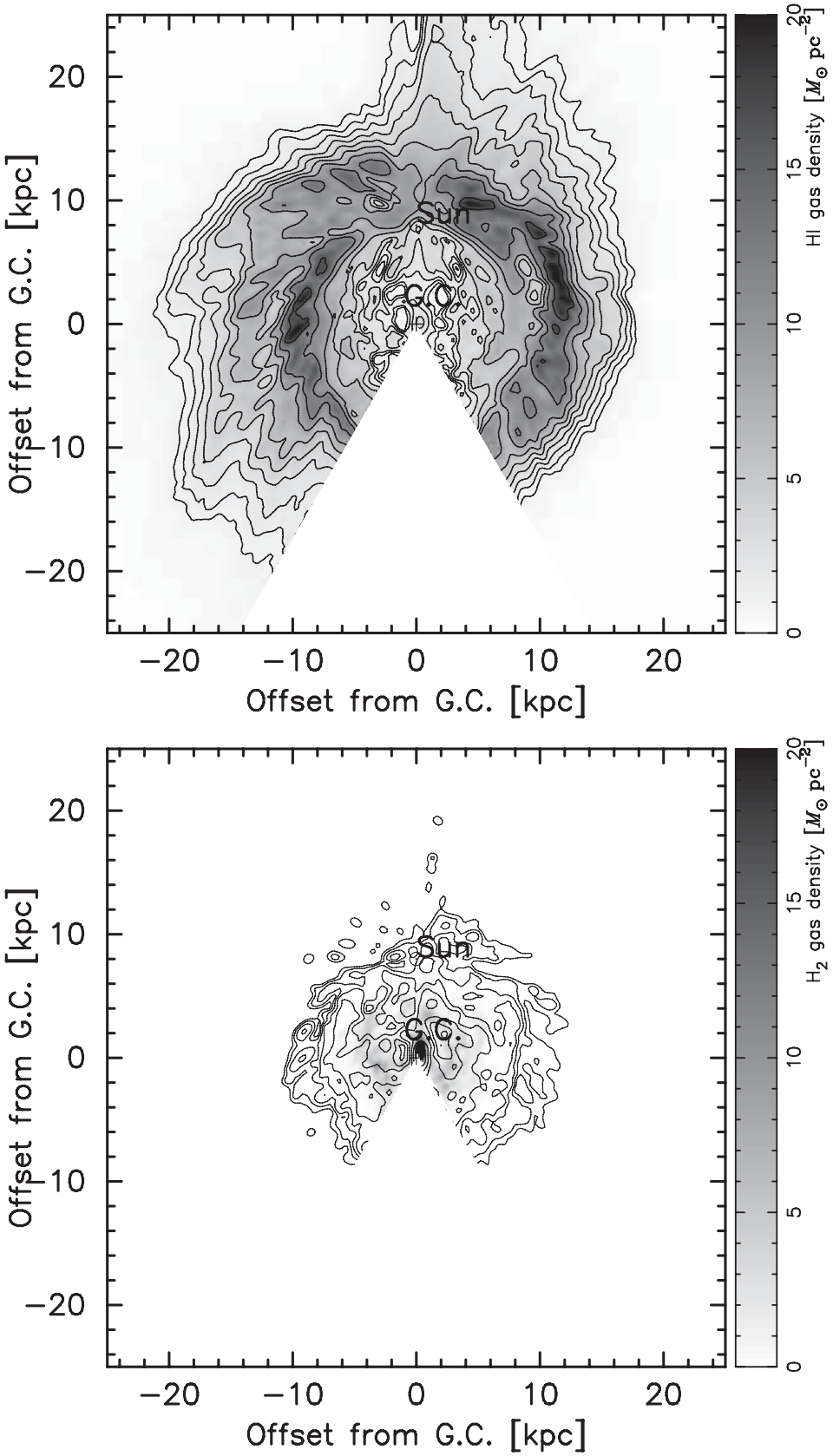


**Fig. 1.** Face-on maps of (top) H I and (bottom) $H_2$ gases. Contour levels are 1.0, 1.4, 2.0, 2.8, 4.0, 5.6, 8.0, 11.3 $M_\odot$ pc$^{-2}$ for the H I map and 0.25, 0.5, 1.0, 2.0, 4.0, 8.0, 16.0 $M_\odot$ pc$^{-2}$ for $H_2$. The area of $|\theta| < 30^\circ$ is masked because the number of points where H I and $H_2$ density are calculated is too small to show the gas distribution.

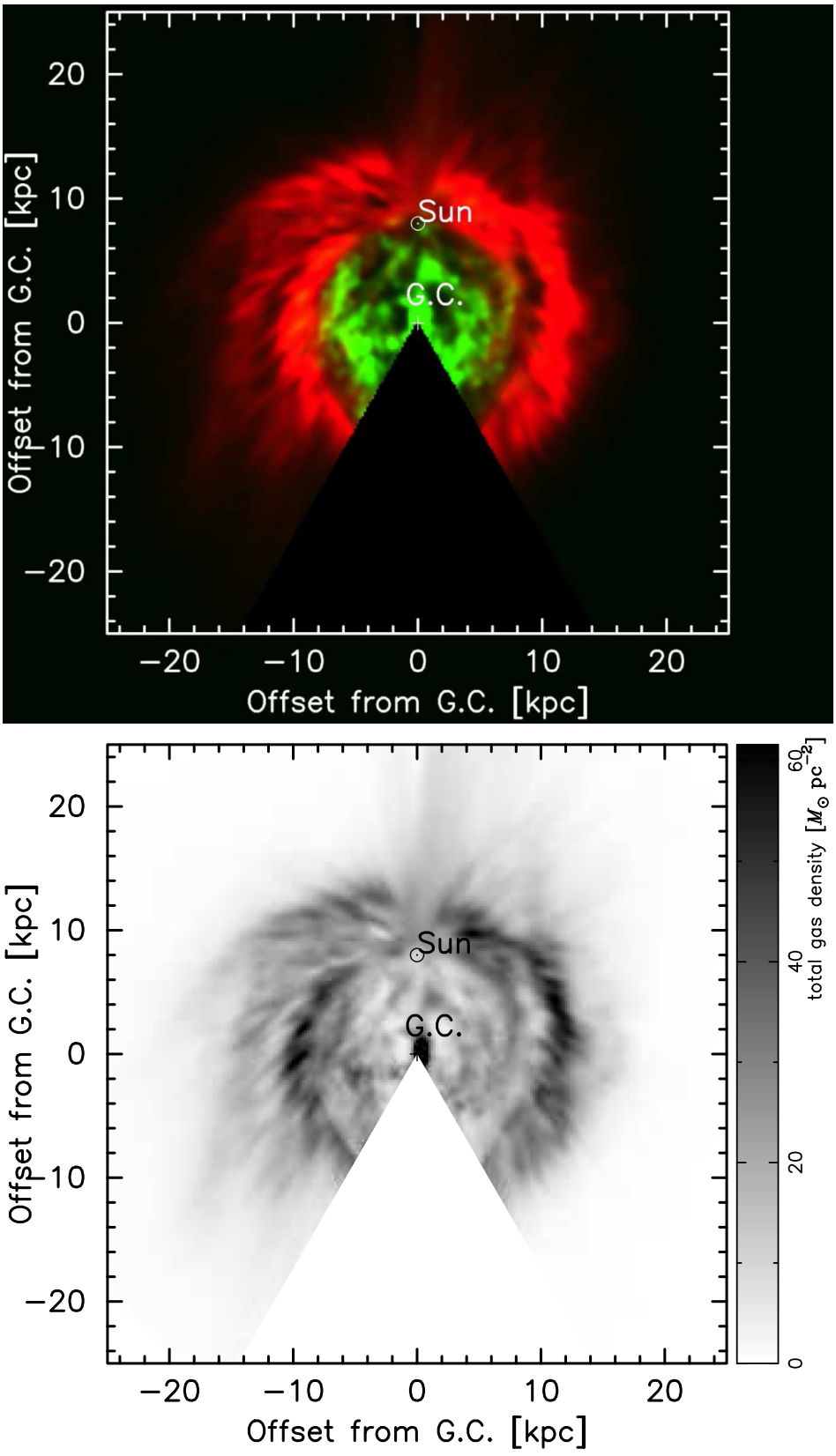


**Fig. 2.** Top: Pseudocolor face-on map of H I (red) and $H_2$ (green) gases. Bottom: Grayscale face-on map of total gas distribution combining H I and $H_2$ densities. (Color online)

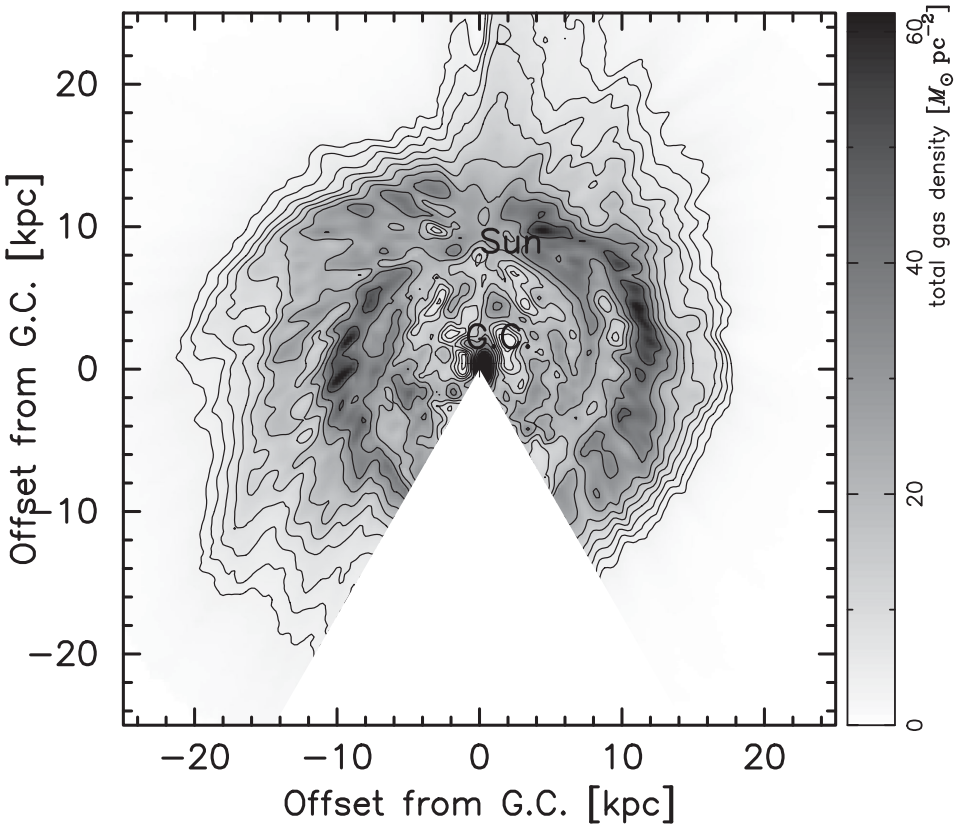


**Fig. 3.** Contour map of the total gas distribution shown in figure 2. Contour levels are 1.0, 1.4, 2.0, 2.8, 4.0, 5.6, 8.0, 11.3, 16.0 $M_\odot$ pc$^{-2}$.

H I and $H_2$ maps. Figure 3 shows a contour map of the total gas map shown in figure 2. These maps are advantageous in tracing global structure such as spiral arms from the inner to the outer parts, since the $H_2$ and H I components preferentially trace the inner and outer arms, respectively. The spiral arms traced here are described in the subsection 4.5.

### 4.2 Radial distribution

The left panel of figure 4 shows the radial distributions of the H I, $H_2$, and the total (H I plus $H_2$) gases in filled circles, open circles, and solid line, respectively. This figure shows that the molecular gas is dominant in the central region and H I gas is dominant in the outer region. The total gas density attains its maximum at the center, with a second peak around $R = 10$ kpc. Beyond $R = 10$ kpc, it decreases with the Galactocentric distance and becomes lower than 1 $M_\odot$ pc$^{-2}$ around $R = 17$ kpc. The dashed line is an exponential function, expressed as $\Sigma(R) = \Sigma_0 e^{-(R-R_0)/R_h}$, where $\Sigma_0 = 30\,M_\odot$ pc$^{-2}$ and $R_h = 3.75$ kpc, adopted from Kalberla and Kerp (2009).

The right panel of figure 4 shows the accumulated gas mass as a function of the Galactocentric distance. The H I and $H_2$ masses within the solar circle are almost the same: $7.5 \times 10^8\,M_\odot$. This result is similar to Bloemen et al. (1986), who estimated the H I and $H_2$ masses to be $9.2 \times 10^8\,M_\odot$ and $9.4 \times 10^8\,M_\odot$, respectively, by comparing high-energy gamma ray emission. Considering the difference in the adopted Galactic constant, their averaged value $9.3 \times 10^8\,M_\odot$ is $9.3/7.5 \times (8/10)^2 = 0.8$ times smaller than our estimation. Kalberla and Dedes (2008) estimated the H I mass within the solar circle to be $1.8 \times 10^9\,M_\odot$. This discrepancy is thought to be caused by the difference in the models adopted to derive H I distribution in the $z$ direction within the solar circle. In our paper, we took a model with a sech$^2$ function, as described in subsection 3.3. On the other hand, Kalberla and Dedes (2008) took a model with the exponential function adopted in Kalberla et al. (2007), which can reproduce the H I distribution at high altitude. The H I surface density and H I mass that we calculated are thought to be underestimated by the amount of the flared H I component, as pointed out by Lockman (1984).

The H I gas reaches a maximum value of $7.2 \times 10^9\,M_\odot$ at the radius of 30 kpc, which is consistent with Kalberla and Kerp (2009) considering the difference in the adopted Galactic constant $R_0$. The $H_2$ reaches a maximum value of $8.5 \times 10^8\,M_\odot$ around the radius of 12 kpc. The total gas mass reaches $8.0 \times 10^9\,M_\odot$ at the radius of 30 kpc. The H I and $H_2$ gas components are 89% and 11% of the total gas mass, respectively.

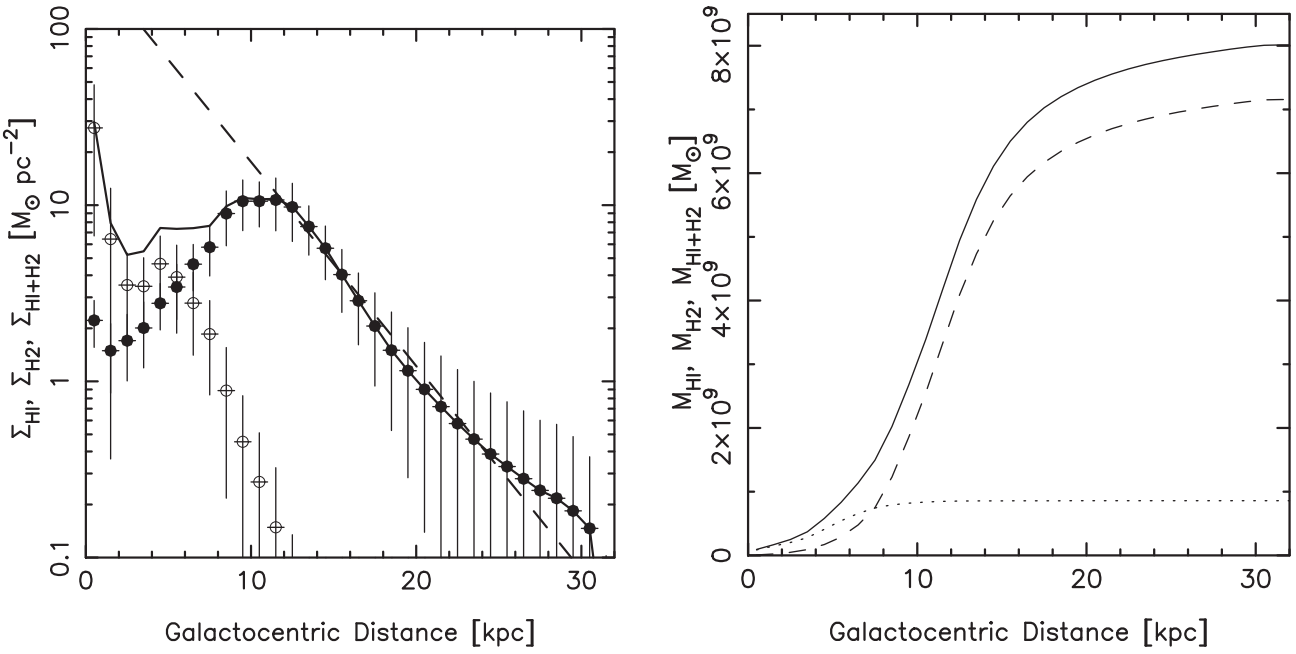


**Fig. 4.** Left: Radial profiles of H I (filled circles), $H_2$ (open circles), and total gas surface densities (thick line). The dashed line is the fitted line taken from Kalberla and Kerp (2009). Right: The accumulated gas mass within each radius. The dashed, dotted, and solid lines denote H I, $H_2$, and total gases, respectively. The $H_2$ and H I components reach their maximum values at the radii of 10 and 30 kpc, respectively.

### 4.3 Vertical cross sections

Figure 5 shows vertical cross sections of the H I and $H_2$ gas distributions. Grayscale and black contours denote the H I density. Red contours represent the $H_2$ gas density. The outer H I layer beyond the Galactocentric distance of 12 kpc is strongly warped as well as the inner H I and $H_2$ layers are corrugated as mentioned in Papers I and II.

The $H_2$ gas disk is thinner than the H I disk; external galaxies show the same characteristics (Scoville et al. 1993). The thickness of the H I gas disk increases with the Galactocentric distance as former works presented (Levine et al. 2006; Kalberla et al. 2007), while the thickness of the $H_2$ gas disk shows a smaller variation (Bronfman et al. 1988; Nakanishi & Sofue 2006).

Figure 5 shows that the peaks of the $H_2$ gas distribution roughly coincide with the H I gas peaks. However, the midplane of the $H_2$ disk is slightly shifted from the H I midplane in some parts, as is clearly seen in the outer disk of $\theta = 120°$–$140°$. This can be interpreted that the molecular gas fraction is not determined only by the pressure, but UV radiation from star-forming regions changes the molecular fraction (Tanaka et al. 2014), or that it is a transient phase, in which the molecular fraction leads to an equilibrium (Nakanishi et al. 2006; Inutsuka et al. 2015).

### 4.4 Thickness of the gas disk

The thickness of the gas layer is measured for each of H I and $H_2$ as shown in figure 6. The thickness of the H I gas layer increases from 100 pc to 2 kpc with the radius, while the thickness of the $H_2$ gas layer slowly increases from 50 pc to 200 pc. These results are consistent with the previous works (Papers I and II). The thin and small $H_2$ disk is embedded in the thicker and more extended H I gas disk as shown in a field galaxy (Crosthwaite et al. 2001).

### 4.5 Spiral arms

The total gas map shown in figure 2 enables us to trace spiral arms from the inner to the outer Galaxy more clearly than ever, by taking advantage of the H I and $H_2$ maps. We can trace the well-known spiral arms such as the Norma–Cygnus, Sagittarius–Carina, Perseus, Scutum–Crux, and Orion arms from the inner to the outer Galaxy as shown in figure 7, which shows schematic tracings of all these spiral arms. All the spiral arms can be traced as logarithmic spiral arms, which are overlaid on the total gas map with thick lines. The pitch angles are in the range of 11°–15°, which is the consistent with the mean value, $13.^\circ1 \pm 0.^\circ6$, of former works shown by Vallée (2015). The directions of tangents to the individual arms are indicated with broken lines. We describe properties of the individual spiral arms in detail below.

#### 4.5.1 Norma–Cygnus arm

The Norma arm refers to the inner part of the spiral arm labelled as No.1. It was originally identified as a spiral arm found in the fourth quadrant in the inner Galaxy. The

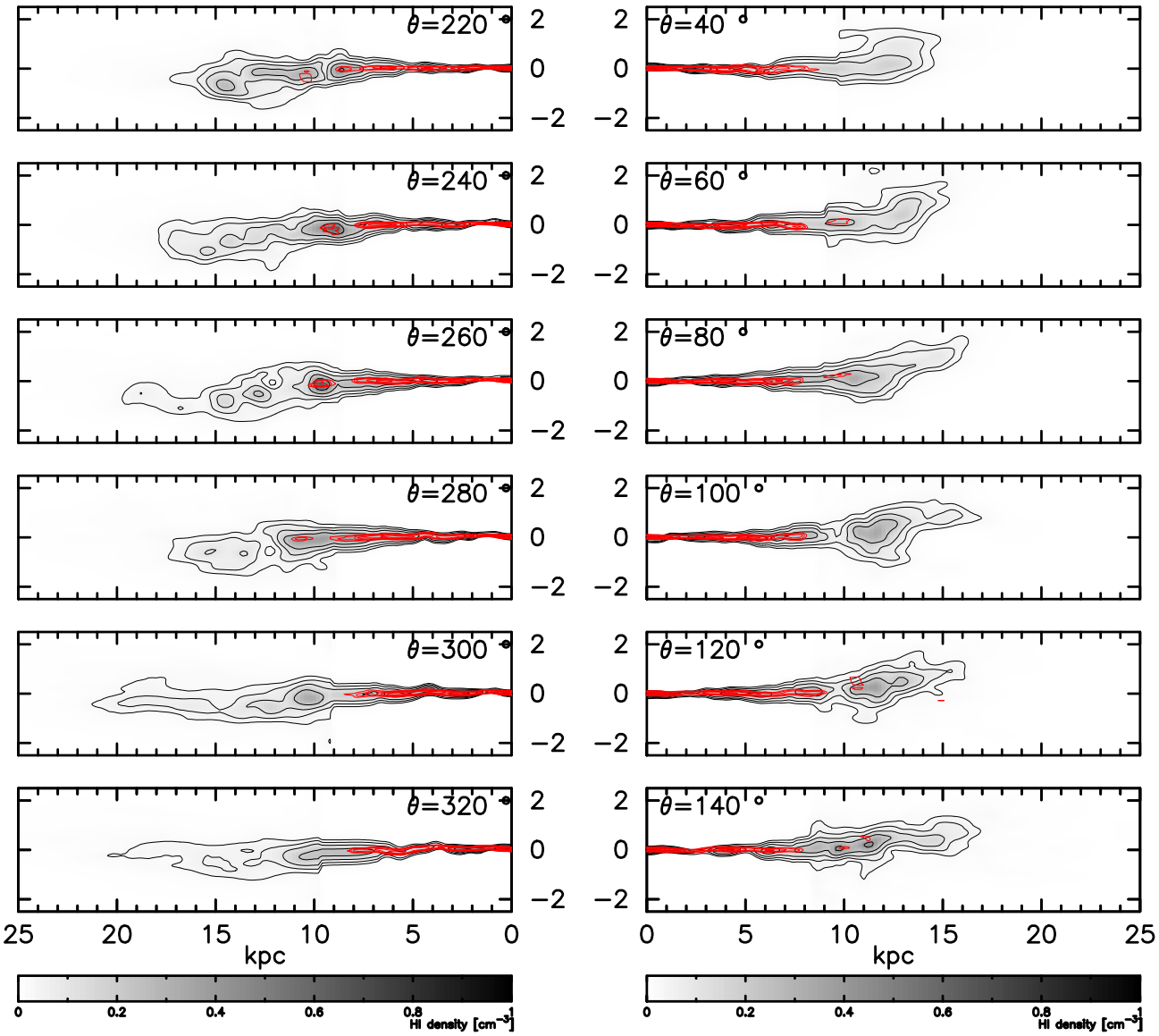


**Fig. 5.** Vertical slices of H I and $H_2$ gas maps. The H I distribution is displayed with grayscale and black contours. The $H_2$ map is presented with red contours. Contour levels are 0.025, 0.05, 0.10, 0.20, and 0.40 $cm^{-3}$. (Color online)

tangents to the Norma arm are found in the direction of $l = 328.^{\circ}5 \pm 3.^{\circ}5$ (Vallée 2014), which corresponds to the direction of the constellation Norma.

The Cygnus arm refers to the outer part of the spiral arm labelled as No.1. The Cygnus arm is also called the Outer arm (Vallée 2014). It is clearly traced in the face-on H I map as one of the most prominent arms in the outermost region, arcing from $(R, \theta) \sim (9\,\mathrm{kpc}, 50^{\circ})$ to $(R, \theta) \sim (11\,\mathrm{kpc}, 120^{\circ})$ as described in Paper II. Recent VLBI observation of the $H_2O$ line in masers traced this spiral as a logarithmic spiral arm with a pitch angle of $13.^{\circ}8 \pm 3.^{\circ}3$ based on the annual parallax (Hachisuka et al. 2015).

As discussed in Paper II, the Norma and Cygnus arms can be identified as the same spiral arm considering that their pitch angles should be 11°–15°. Hence, we call this arm the Norma–Cygnus arm and label it as No.1 in figure 7, where a schematic tracing of the Norma–Cygnus arm is presented by a logarithmic spiral arm starting at $(R, \theta) = (2.6\,\mathrm{kpc}, -210^{\circ})$ and ending at $\theta = 130^{\circ}$ with a pitch angle of 15°. Its origin is considered to coincide with the "near 3 kpc arm" and to connect to the the near side of the Galactic bar (Vallée 2014). The parameters describing all the arms are summarized in table 1. This picture is consistent with the recent panoramic view obtained in a compilation of former works (Vallée 2005).

### 4.5.2 Perseus arm

The Perseus arm, labelled as No.2, is known as one of the most prominent arms (Georgelin & Georgelin 1976). It is found in the range of $\theta = 30^{\circ}$–$230^{\circ}$, and is prominent in the

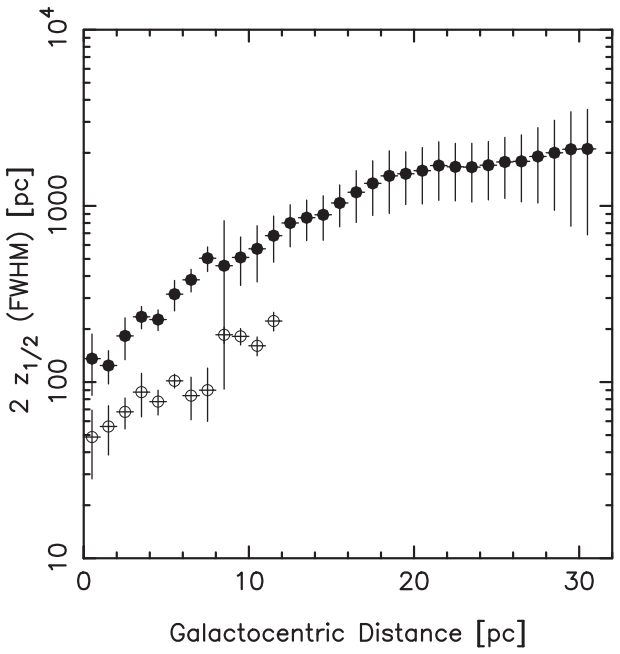


**Fig. 6.** Thickness of the H I (filled circle) and $H_2$ (open circle) gas layers measured with $2z_{1/2}$ (FWHM) versus the Galactocentric distance.

outer Galaxy. The Perseus arm can be traced with a logarithmic spiral arm with a pitch angle of 15°. In figure 7, a schematic tracing of the Perseus arm is shown by a logarithmic spiral arm starting at $(R, \theta) = (2.9\,\mathrm{kpc}, -120°)$ with a pitch angle of 15° and ending at $\theta = 260°$.

Vallée (2014) compiled the former works and concluded that the Perseus arm starts in the direction of $l = 336.^{\circ}9 \pm 0.^{\circ}7$, while Churchwell et al. (2009) concluded that the Perseus arm starts at the far edge of the central bar. If we assume that the Perseus arms starts at the far edge of the central bar, the major radius of the central bar needs to be 5 kpc, considering the pitch angle and its distance measured around the Sun. However, the size of the bar and expected non-circular motion is inconsistent with former works. Our study supports the picture that the Perseus arm starts at $l = 336.^{\circ}9 \pm 0.^{\circ}7$ and not from the either edge of the central bar, as concluded by Vallée (2014).

#### 4.5.3 Sagittarius–Carina arm

The Sagittarius–Carina arm, labelled as No.3, is known as the closest spiral arm to the Sun. The tangents to the Sagittarius and Carina arms are found in the directions of $l = 48.^{\circ}5 \pm 2.^{\circ}5$ and $l = 284.^{\circ}5 \pm 2.^{\circ}5$, which correspond to the directions of the Sagittarius and Carina constellations, respectively (Vallée 2014).

In this study, the side of the Carina arm can be clearly traced in the H I and total gas maps and is well fitted by a logarithmic spiral arm with a pitch angle of 11°, though the side of the Sagittarius arm is less prominent, as mentioned in Paper II. In figure 7, a schematic tracing of this arm is presented by a logarithmic spiral arm starting at $(R, \theta) = (4.2\,\mathrm{kpc}, 30°)$ with a pitch angle of 11° and ending at $\theta = 310°$.

#### 4.5.4 Scutum–Crux arm

The Scutum–Crux arm, labelled as No.4, is found between the Norma–Cygnus and the Sagittarius–Carina arms as indicated in figure 7. Similarly to the Sagittarius–Carina arm, the tangent to the Scutum and Crux arms are found in the directions of $l = 33.^{\circ}2 \pm 17.^{\circ}2$ and $l = 309.^{\circ}3 \pm 0.^{\circ}9$ (Vallée 2014), which correspond to the directions of the Scutum and Crux constellations, respectively. The Crux arm is often referred to as the Centaurus arm and so the Scutum–Crux arm is often called the Scutum–Centaurus arm (Churchwell et al. 2009).

In the first quadrant, the separation between the Scutum–Crux and Sagittarius–Carina arms gets small and they seem to form a ring-like structure, which was reported to exist at the Galactocentric radius of $R_0/2$ (Clemens et al. 1988).

This arm can be traced by a logarithmic spiral arm with a pitch angle of 11°. Considering its pitch angle, it is thought to connect to the distant molecular arm found by Dame and Thaddeus (2011), as they concluded. In figure 7, a schematic tracing of the Scutum–Crux arm is shown by a logarithmic spiral arm starting at $(R, \theta) = (2.6\,\mathrm{kpc}, -30°)$ and ending at $\theta = 430°$ with a pitch angle of 11°.

#### 4.5.5 Orion arm

Between the Sagittarius–Carina and Perseus arms, there exists a less prominent but clear spiral arm, where the Sun is located, as shown in figure 7. This spiral arm is referred to as the Orion arm or the Local arm (Bobylev & Bajkova 2014). In figure 7, a schematic tracing of the Local arm is presented by a logarithmic spiral arm starting at $(R, \theta) = (7.0\,\mathrm{kpc}, 130°)$ and ending at $\theta = 290°$ with a pitch angle of 15°.

So far, there are two possibilities on the structure of the Orion arm: (1) it is a bridge-like structure connecting the Sagittarius–Carina and Perseus arms (Weaver 1970; Churchwell et al. 2009), or (2) it is a normal spiral arm with a similar pitch angle to the others. Our result supports the latter picture, which is is consistent with the recent VLBI result concluded by Xu et al. (2013) and Bobylev and Bajkova (2014), who measured annual parallaxes of 23–25 high-mass star formation regions with VLBA to show that the Orion arm is traced with a logarithmic spiral arm with a pitch angle of $12.^{\circ}9 \pm 2.^{\circ}9$–$13.^{\circ}8 \pm 3.^{\circ}3$.

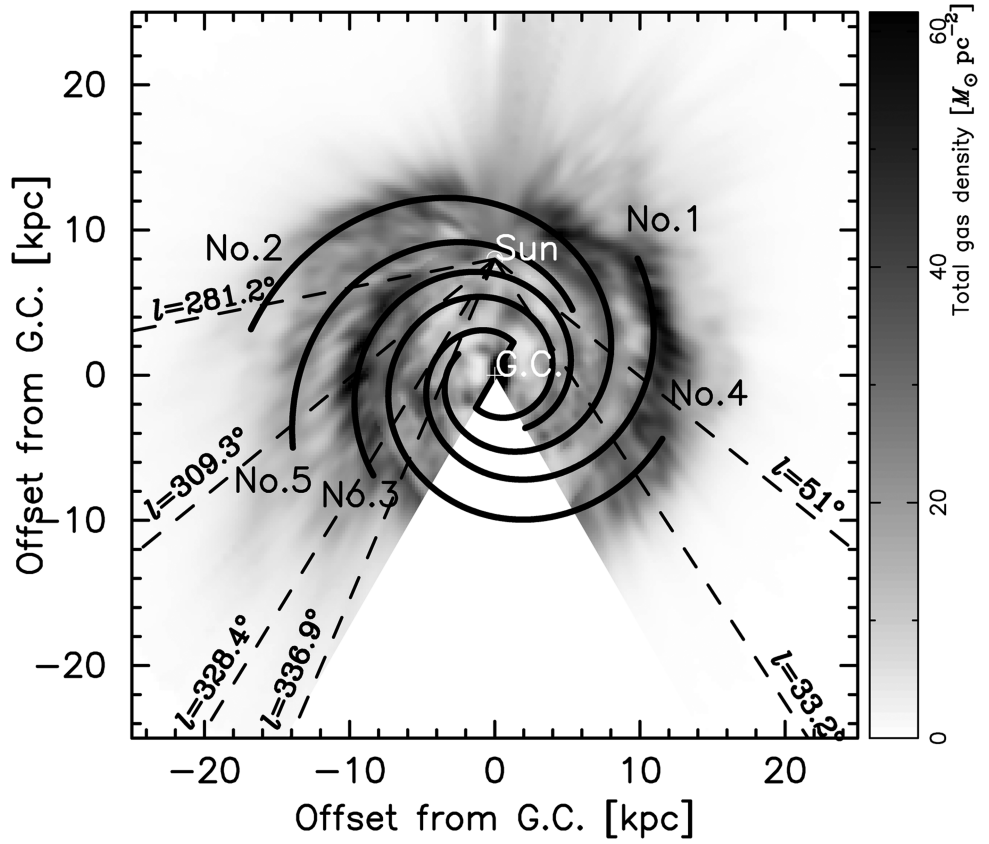


**Fig. 7.** Schematic tracers of spiral arms superimposed on the total gas distribution map. No.1: Norma–Cygnus arm; No.2: Perseus arm; No.3: Sagittarius–Carina arm; No.4: Scutum–Crux arm; No.5: Orion (Local) arm. The dashed lines are tangents to the inner spiral arms.

**Table 1.** Parameters of spiral arms.

| Name | Pitch angle (°) | Beginning radius (kpc) | Beginning angle (°) | Ending angle (°) |
|---|---|---|---|---|
| Norma–Cygnus (Outer) | 15 | 2.6 | − 210 | 130 |
| Perseus | 15 | 2.9 | − 120 | 260 |
| Sagittarius–Carina | 11 | 4.2 | 30 | 310 |
| Scutum–Crux | 11 | 2.6 | − 30 | 430 |
| Orion (Local) | 15 | 7.0 | 130 | 290 |

### 4.6 Molecular fraction

To quantitatively investigate the physical properties of the ISM, we define a parameter $f_{\rm mol}$ as

$$f_{\rm mol} = \frac{\Sigma_{\rm H_2}}{\Sigma_{\rm HI} + \Sigma_{\rm H_2}}, \quad (6)$$

where $\Sigma_{\rm HI}$ and $\Sigma_{\rm H_2}$ are the surface densities of the HI and $H_2$ gases, respectively. Figure 8 shows $f_{\rm mol}$ plotted versus Galactocentric distance. The molecular fraction $f_{\rm mol}$ is above 0.5 in the Galactocentric range of ($R < 5$ kpc), which implies that $H_2$ gas is dominant in this range. The molecular fraction $f_{\rm mol}$ rapidly decreses beyond $R = 5$ kpc and becomes less than 0.1 in the outer Galaxy ($R > 8$ kpc), which implies that HI gas is dominant in the outer disk.

Figure 9 shows a map of two-dimensional $f_{\rm mol}$ distribution. In figure 9 we superimposed schematic tracings of spiral arms with gray lines. These spiral arms are the same as those described in subsection 4.1. In addition to the global variation, local variations of the molecular fraction are found. The molecular fraction $f_{\rm mol}$ tends to increase along the spiral arms rather than the inter-arm regions. The molecular fraction $f_{\rm mol}$ varies by 0.1–0.2 between an arm and the inter-arm regions. This tendency is also found in external galaxies (Kuno et al. 1995).

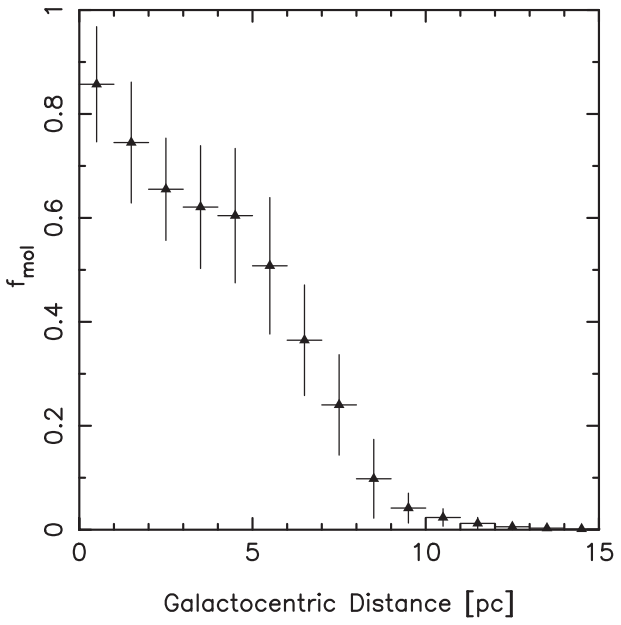


**Fig. 8.** Radial variation of the molecular fraction ($f_{\rm mol}$) obtained by azimuthally averaging the two-dimensional $f_{\rm mol}$ map.

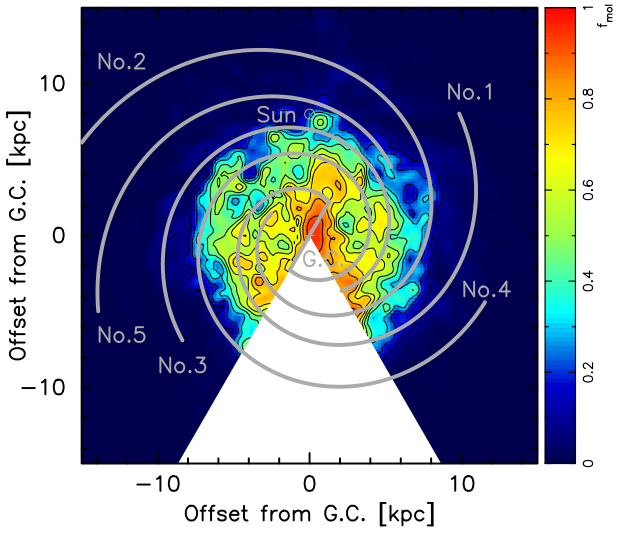


**Fig. 9.** Two-dimensional molecular fraction ($f_{\rm mol}$) map calculated with H I and $H_2$ surface densities. The molecular fraction $f_{\rm mol}$ is defined as $f_{\rm mol} = \Sigma_{H_2}/(\Sigma_{\rm HI} + \Sigma_{H_2})$. The schematic tracers of spiral arms are indicated with gray lines. (Color online)

## 5 Possible uncertainties

We adopted several assumptions for simplicity in obtaining the gaseous maps. In this section, we note possible systematic errors caused by such assumptions.

### 5.1 Kinematic distance

The kinematic distance, which we adopted as a distance estimator, is based on the assumption that the Galactic rotation is purely circular. However, it is known that non-circular motion exists and affects the kinematic distance.

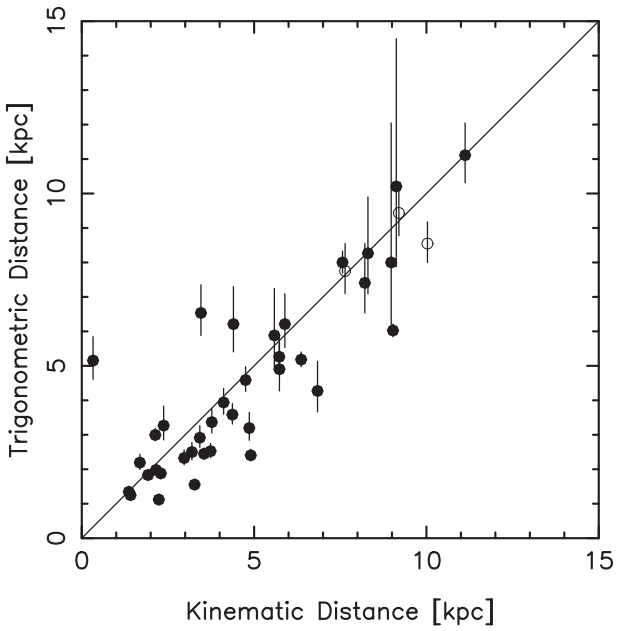


**Fig. 10.** Comparison of kinematic distance used in this paper and trigonometric distance obtained with VLBI observation (Reid et al. 2014). Open and filled circles indicate sources within the Galactocentric distance of 3 kpc, and the others, respectively.

There have been a lot of measurements of annual parallaxes with VLBI, which have shown that the typical error is within a few kpc (Hachisuka et al. 2009; Sakai et al. 2012; Nakanishi et al. 2015). Figure 10 shows a comparison of VLBI trigonometric distance taken from Reid et al. (2014) and the kinematic distance used in this paper. Open and filled circles indicate sources within the Galactocentric distance of 3 kpc, and the others, respectively. If both values are the same, the data are plotted on the solid line.

The standard deviation between trigonometric and kinematic distances is calculated to be 2.3 kpc, which is a typical error in heliocentric distance of the maps shown in this paper. This value is consistent with results from the recent *N*-body + hydrodynamical simulation shown by Baba et al. (2009), who concluded that kinematic distance had an error of 2–3 kpc.

Figure 10 shows that there is no big difference between the filled and open circles, though the non-circular motion is significant near the Galactic center (e.g., Sawada et al. 2004). Therefore, the typical error in the kinematic distance of the sources within the Galactocentric distance of 3 kpc is of the same order as the other sources located in the outer region.

### 5.2 Galactic constant

The Galactic constants ($R_0$, $V_0$) change the kinematic distance, according to equation (1). Since the Galactocentric distance of a gas cloud having LSR velocity $V_{\rm LSR}$ in the direction of galactic longitude $l$ is calculated to be $R = R_0/\{[V_{\rm LSR}/V(R)\sin l] + [V_0/V(R)]\}$, the solar Galactocentric distance $R_0$ essentially scales the size but not the shape of the gaseous disk. The surface density changes by the square of $R_0$.

Though the solar rotational velocity $V_0$ can change the kinematic distance, it is of the order of $V_0/V(R)$, which is typically less than 25% as estimated from fluctuations of the rotation curve (Sofue et al. 2009).

### 5.3 Fitting method

In order to divide the mixed emission from near and far points of the inner Galaxy, we utilized the fitting method explained in subsection 3.3. However, it is not necessarily perfect because the actual HI vertical distribution cannot be expressed with a single function (Lockman 1984). The difference in midplane density between the data and the model is typically less than 20%–30%, as mentioned in Paper II.

### 5.4 Optical thickness

In this study, we assume that the HI line is optically thin for simplicity in measuring the HI column density. However, recent studies point out that HI mass is underestimated by factor of 2–2.5 when the HI line is assumed to be optically thin (Fukui et al. 2014, 2015).

## 6 Summary

In this paper, we showed three-dimensional HI and $H_2$ maps of the Milky Way galaxy using the latest HI and CO survey data and rotation curves based on the kinematic distance. The HI map has been revised with improved analysis from Paper I.

Comparing the HI and $H_2$ maps, it was shown that the $H_2$ gas is distributed mainly inside the solar circle while HI distribution is extended to the large Galactocentric distance of 15–20 kpc, and its outskirts are asymmetric about the Galactic center. The radial distribution of total gas density generally decreases with the Galactocentric distance, peaking at the center, while it is roughly constant between 5 and 10 kpc. The total gas mass is $8 \times 10^9\,M_\odot$, 89% and 11% of which are HI and $H_2$ gas masses, respectively. The $H_2$ gas layer is embedded in the thicker and more extended HI layer. The HI layer is largely bent at the Galactocentric distance of 12 kpc, as well as corrugated in the inner Galaxy.

We show the total gas density map of the Milky Way galaxy for the first time by summing the HI and $H_2$ gas density maps. It proves more advantageous in tracing spiral arms from the center to the outer Galaxy than the individual HI and $H_2$ maps. We could easily trace five logarithmic spiral arms in the total gas map: the Norma–Cygnus, Perseus, Sagittarius–Carina, Scutum–Crux, and Orion arms. The Norma and the Cygnus arms are identified as the same spiral arm, considering their pitch angles of 11°–15°.

The fraction of molecular component to total gas decreases with the Galactocentric distance and drops steeply in the small radius range of 5–8 kpc. The two-dimensional molecular fraction map shows that it is also locally enhanced on the spiral arms.

## Acknowledgments

We would like to thank the referee for carefully reading the manuscript. This work was supported by JSPS KAKENHI Grant Number 26800104.

## References

Arimoto, N., Sofue, Y., & Tsujimoto, T. 1996, PASJ, 48, 275
Baba, J., Asaki, Y., Makino, J., Miyoshi, M., Saitoh, T. R., & Wada, K. 2009, ApJ, 706, 471
Bajaja, E., Arnal, E. M., Larrarte, J. J., Morras, R., Pöppel, W. G. L., & Kalberla, P. M. W. 2005, A&A, 440, 767
Beuermann, K., Kanbach, G., & Berkhuijsen, E. M. 1985, A&A, 153, 17
Bitran, M., Alvarez, H., Bronfman, L., May, J., & Thaddeus, P. 1997, A&AS, 125, 99
Bloemen, J. B. G. M., et al. 1986, A&A, 154, 25
Bobylev, V. V., & Bajkova, A. T. 2014, Astron. Lett., 40, 783
Broeils, A. H., & van Woerden, H. 1994, A&AS, 107, 129
Bronfman, L., Alvarez, H., Cohen, R. S., & Thaddeus, P. 1989, ApJS, 71, 481
Bronfman, L., Cohen, R. S., Alvarez, H., May, J., & Thaddeus, P. 1988, ApJ, 324, 248
Burton, W. B., & Liszt, H. S. 1983, A&AS, 52, 63
Caswell, J. L., et al. 2011, MNRAS, 417, 1964
Chen, W., Gehrels, N., Diehl, R., & Hartmann, D. 1996, A&AS, 120, 315
Churchwell, E., et al. 2009, PASP, 121, 213
Clemens, D. P. 1985, ApJ, 295, 422
Clemens, D. P., Sanders, D. B., & Scoville, N. Z. 1988, ApJ, 327, 139
Cohen, R. S., Grabelsky, D. A., May, J., Alvarez, H., Bronfman, L., & Thaddeus, P. 1985, ApJ, 290, L15
Crosthwaite, L. P., Turner, J. L., Hurt, R. L., Levine, D. A., Martin, R. N., & Ho, P. T. P. 2001, AJ, 122, 797

Dame, T. M., et al. 1987, ApJ, 322, 706
Dame, T. M., Elmegreen, B. G., Cohen, R. S., & Thaddeus, P. 1986, ApJ, 305, 892
Dame, T. M., Hartmann, D., & Thaddeus, P. 2001, ApJ, 547, 792
Dame, T. M., & Thaddeus, P. 2008, ApJ, 683, L143
Dame, T. M., & Thaddeus, P. 2011, ApJ, 734, L24
Dehnen, W., & Binney, J. 1998, MNRAS, 294, 429
Downes, D., Wilson, T. L., Bieging, J., & Wink, J. 1980, A&AS, 40, 379
Drimmel, R., & Spergel, D. N. 2001, ApJ, 556, 181
Fukui, Y., et al. 2014, ApJ, 796, 59
Fukui, Y., Torii, K., Onishi, T., Yamamoto, H., Okamoto, R., Hayakawa, T., Tachihara, K., & Sano, H. 2015, ApJ, 798, 6
Georgelin, Y. M., & Georgelin, Y. P. 1976, A&A, 49, 57
Grabelsky, D. A., Cohen, R. S., Bronfman, L., Thaddeus, P., & May, J. 1987, ApJ, 315, 122
Hachisuka, K., Brunthaler, A., Menten, K. M., Reid, M. J., Hagiwara, Y., & Mochizuki, N. 2009, ApJ, 696, 1981
Hachisuka, K., Choi, Y. K., Reid, M. J., Brunthaler, A., Menten, K. M., Sanna, A., & Dame, T. M. 2015, ApJ, 800, 2
Hartmann, D., & Burton, W. B. ed. 1997, Atlas of Galactic Neutral Hydrogen (Cambridge, UK: Cambridge University Press), 243
Heiles, C. 1979, ApJ, 229, 533
Honma, M., Sofue, Y., & Arimoto, N. 1995, A&A, 304, 1
Imamura, K., & Sofue, Y. 1997, A&A, 319, 1
Inutsuka, S., Inoue, T., Iwasaki, K., & Hosokawa, T. 2015, A&A, 580, A49
Kalberla, P. M. W., Burton, W. B., Hartmann, D., Arnal, E. M., Bajaja, E., Morras, R., & Pöppel, W. G. L. 2005, A&A, 440, 775
Kalberla, P. M. W., & Dedes, L. 2008, A&A, 487, 951
Kalberla, P. M. W., Dedes, L., Kerp, J., & Haud, U. 2007, A&A, 469, 511
Kalberla, P. M. W., & Kerp, J. 2009, ARA&A, 47, 27
Kerr, F. J. 1969, ARA&A, 7, 39
Kerr, F. J., Bowers, P. F., Jackson, P. D., & Kerr, M. 1986, A&AS, 66, 373
Kuno, N., Nakai, N., Handa, T., & Sofue, Y. 1995, PASJ, 47, 745
Levine, E. S., Blitz, L., & Heiles, C. 2006, ApJ, 643, 881
Lockman, F. J. 1984, ApJ, 283, 90
McClure-Griffiths, N. M., Dickey, J. M., Gaensler, B. M., & Green, A. J. 2004, ApJ, 607, L127
May, J., Bronfman, L., Alvarez, H., Murphy, D. C., & Thaddeus, P. 1993, A&AS, 99, 105
Muller, C. A., & Westerhout, G. 1957, Bull. Astron. Inst. Netherland, 13, 151
Myers, P. C. 1978, ApJ, 225, 380
Myers, P. C., Dame, T. M., Thaddeus, P., Cohen, R. S., Silverberg, R. F., Dwek, E., & Hauser, M. G. 1986, ApJ, 301, 398
Nakanishi, H., et al. 2006, ApJ, 651, 804
Nakanishi, H., et al. 2015, PASJ, 67, 68
Nakanishi, H., & Sofue, Y. 2003, PASJ, 55, 191 (Paper I)
Nakanishi, H., & Sofue, Y. 2006, PASJ, 58, 847 (Paper II)
Nishiyama, K., Nakai, N., & Kuno, N. 2001, PASJ, 53, 757
Oort, J. H., Kerr, F. J., & Westerhout, G. 1958, MNRAS, 118, 379
Reid, M. J., et al. 2014, ApJ, 783, 130
Sakai, N., Honma, M., Nakanishi, H., Sakanoue, H., Kurayama, T., Shibata, K. M., & Shizugami, M. 2012, PASJ, 64, 108
Sanders, D. B., Clemens, D. P., Scoville, N. Z., & Solomon, P. M. 1986, ApJS, 60, 1
Sanders, D. B., Solomon, P. M., & Scoville, N. Z. 1984, ApJ, 276, 182
Sawada, T., Hasegawa, T., Handa, T., & Cohen, R. J. 2004, MNRAS, 349, 1167
Scoville, N. Z., Thakkar, D., Carlstrom, J. E., & Sargent, A. I. 1993, ApJ, 404, L59
Sofue, Y., Honma, M., & Arimoto, N. 1995, A&A, 296, 33
Sofue, Y., Honma, M., & Omodaka, T. 2009, PASJ, 61, 227
Spitzer, L., Jr. 1942, ApJ, 95, 329
Tanaka, A., Nakanishi, H., Kuno, N., & Hirota, A. 2014, PASJ, 66, 66
Taylor, J. H., & Cordes, J. M. 1993, ApJ, 411, 674
Vallée, J. P. 2005, AJ, 130, 569
Vallée, J. P. 2014, ApJS, 215, 1
Vallée, J. P. 2015, MNRAS, 450, 4277
van de Hulst, H. C., Muller, C. A., & Oort, J. H. 1954, Bull. Astron. Inst. Netherland, 12, 117
Verschuur, G. L. 1973, A&A, 22, 139
Wakker, B. P., & van Woerden, H. 1997, ARA&A, 35, 217
Weaver, W. B. 1970, AJ, 75, 938
Xu, Y., et al. 2013, ApJ, 769, 15